COMMUNICATION
Flexible Electronics
NANO · MICRO small
www.small-journal.co

High Performance, Tunable Electrically Small Antennas through Mechanically Guided 3D Assembly

*Fei Liu, Ying Chen, Honglie Song, Fan Zhang, Zhichao Fan, Yuan Liu, Xue Feng, John A. Rogers, Yonggang Huang, and Yihui Zhang**

To address demands for increased data transmission rates, electrically small antennas (ESAs) that simultaneously offer large frequency bandwidths and small physical sizes are of growing interest. 3D layouts are particularly important in this context and among various 3D ESAs, systems that adopt hemispherical shapes are very promising, because they can occupy the entire Chu-sphere and offer outstanding electrical performance. Researchers have developed a few different approaches to fabricate high-quality hemispherical ESAs, but most have static layouts and fixed operating frequencies. Here, a mechanically guided 3D assembly approach is introduced for the design and fabrication of deformable hemispherical ESAs that can offer tunable, dynamic properties to adapt to changes in environmental conditions. The strategy exploits controlled compressive buckling of strategically patterned 2D precursor structures, as a low-cost and high-yield scheme that can exploit conventional, planar processing technologies and commercially available platforms. Combined numerical simulations and experimental measurements show outstanding performance characteristics in terms of the quality factor and radiation efficiency. Application of external tensile strains to elastomeric substrates for these systems allows them to be reshaped and reversibly tuned through a wide range of center frequencies. Mechanical testing under different loading conditions demonstrates the ability of these ESAs to accommodate large deformations.

As mobile/wearable devices with wireless data communication capabilities become increasingly miniaturized, sophisticated, and ubiquitous,[1–7] the interest in the development of antennas with large bandwidths and small sizes grows. Extensive academic and industrial studies focus on various designs for high efficiency electrically small antenna (ESA). An antenna is considered electrically small when its electrical size is less than 0.5, as defined by the value of ka, where k is the free space wavenumber ($k = 2\pi a/\lambda$, with λ being the wavelength) at the operating frequency, and a is the radius of the smallest sphere that circumscribes the antenna. The quality factor (Q), given by the ratio of stored energy to radiated energy, is one of the most important metrics for the ESAs.[8] A design goal is to achieve both a high radiation efficiency η_{eff} and a low Q. The Chu-limit defines a fundamental lower bound for Q, given by $Q_{\text{lb}} = \eta_{\text{eff}}[(1/ka)^3 + 1/(ka)]$, where ka is the electrical size.[9–11] This equation shows that the minimum attainable Q increases rapidly as ka decreases, thereby establishing practical challenges in the design of ESAs. The ratio Q/Q_{lb}, takes both Q and η_{eff} into account, and is, therefore, a widely used metric for the performance of ESAs.[12–16]

ESAs can be classified into two categories (planar and volumetric ESAs) according to the different geometries. Planar ESAs generally have limited efficiencies and bandwidths, due to their small volume occupation of the Chu-sphere. Volumetric ESAs overcome these limitations by offering relatively large volume occupation of the Chu-sphere, with resulting capabilities to substantially improve the performance.[17] Among various designs in volumetric ESAs, those with spherical and/or hemispherical geometries can occupy the entire Chu-sphere, with the

---

F. Liu, Dr. H. Song, Dr. F. Zhang, Dr. Z. Fan, Y. Liu,
Prof. X. Feng, Prof. Y. Zhang
AML
Department of Engineering Mechanics
Center for Flexible Electronics Technology
Center for Mechanics and Materials
Tsinghua University
Beijing 100084, China
E-mail: yihuizhang@tsinghua.edu.cn

Dr. Y. Chen
Institute of Flexible Electronics Technology of THU
Zhejiang, Jiaxing 314000, China

The ORCID identification number(s) for the author(s) of this article can be found under https://doi.org/10.1002/smll.201804055.

DOI: 10.1002/smll.201804055

Prof. J. A. Rogers
Departments of Materials Science and Engineering
Biomedical Engineering
Chemistry, Neurological Surgery
Mechanical Engineering
Electrical Engineering and Computer Science
Simpson Querrey Institute & Feinberg Medical School
Center for Bio-Integrated Electronics
Northwestern University
Evanston, IL 60208, USA

Prof. Y. Huang
Departments of Civil and Environmental Engineering
Mechanical Engineering
Materials Science and Engineering
Northwestern University
Evanston, IL 60208, USA

potential to achieve the lowest $Q/Q_{\rm lb}$.[18] The fabrication of volumetric ESAs, especially the (hemi)spherical ones, is, however, much more challenging than that for planar ESAs. For decades, researchers have sought routes to precise, low-cost, scalable production of (hemi)spherical ESAs. The simplest approach involves manually bending wires into desired configurations, but this method is intrinsically slow, labor intensive, and it offers limited accuracy in geometric control.[12,17] 3D printing techniques offer impressive capabilities for rapid prototyping and can be exploited to realize hemispherical ESA,[13,19–22] but significant increases in throughput are needed for massive production. The relatively low conducitivity (e.g., ≈30% of those based on deposition techniques) of the printed metallic materials represents an additional challenge to achieving high antenna efficiencies. Another scheme relies on direct transfer patterning as a multistep process to form ESAs on hemispherical substrates, starting with preparation of a mold, transferring metallic structures, followed by etching with a pulsed argon plasma and electroplating to complete the fabrication.[14] This approach is interesting, but issues in process time, cost, and complexity require additional attention. Alternative schemes could offer important options, in this broader context, including those that offer additional capabilities in mechanical tunability to address requirements in wearable electronics and other areas. Designs based on liquid metal alloys and pressure induced tuning are of interest, although potential for leakage of both the alloy and the gas may present practical challenges.[15]

Here we leverage recently developed techniques in mechanical-guided 3D assembly to design and fabricate tunable hemispherical ESAs. This approach exploits well-developed semiconductor technologies to form 2D precursor structures that are then transformed into desired 3D configurations by controlled compressive buckling, in a deterministic manner consistent with predictive models based on finite element analysis (FEA).[23–27] This scheme is appealing, compared with other 3D forming/assembly techniques,[19,28–34] for its applicability to nearly any type of materials including semiconductors, metals, polymers, and their combinations, over length scales spanning from sub-micrometer to meter dimensions.[35] This work demonstrates the utility of this assembly approach to achieve two different types of high-quality ESAs, meanderline-based hemispherical ESA (MHESA) and helix-based hemispherical ESA (HHESA), both of which have $Q/Q_{\rm lb}$ very close to 1. Combined studies based on experimental measurements, mechanics modeling and electromagentic simulations illustrate the key performance characteristics and the reversible tunability of the operating frequency. Cyclic testing under typical mechanical loads demonstrates the robustness of these devices and their ability to sustain extreme deformations. These results suggest simple, low-cost routes to mass production of high-performance, deformable ESAs, with diverse potential applications, including those in wearable and biointegrated electronics.

Figure 1a provides a schematic illustration of the fabrication process for the MHESA (see the Experimental Section for details). The 2D precursor design (Figure 1b) exploits a central-symmetric polyimide (PI, 25 µm in thickness) support with eight arms that connect at the center, for transformation into a 3D shell that approximates the hemispherical shape. The boundary line of each arm follows an arc shape, as detailed in Figure S1 (Supporting Information), such that a nearly closed 3D shape forms as a result of the 3D assembly process. The metal traces (copper, Cu) adopt meander line shapes to make full use of the area, while providing a high degree of design flexiblity. In this example (Figure 1b), the width and spacing of the meander lines are 150 and 500 µm, respectively. Such patterned bilayers of Cu and PI are processed by automatic mechanical cutting, followed by photolithographic wet etching. The entire device consists of two separate components, including the antenna (upper Cu/PI bilayer) and the star-like feed trace (lower Cu/PI bilayer, 750 µm in width), as shown in Figure 1c in an exploded view. Conductive silver paste supports electrical connection between the antenna and the feed trace at the bonding sites. With equal biaxial prestrain ($\varepsilon_{\rm pre} = 41\%$), the compressive forces that result from the release of the elastomer (Dragon Skin, Smooth-On) substrate trigger lateral buckling of the 2D precursor structure, leading to the formation of a 3D hemispherical ESA. This MHESA connects with a SubMiniature version A (SMA) interface at the center of the lower-layer feed trace for energy feeding, noting that the eight upper-layer meander lines do not connect with each other, as schematically illustrated in Figure 1c,d. Figure 1e shows an optical image of the MHESA, with comparison to the results of FEA (see the Experimental Section for details). Without any fitting parameters, the FEA predictions agree well with the experiment. The final 3D configuration is very close to a hemisphere, as evidenced by the sectional profile (Figure 1f, right bottom) that matches well with an ideal semi-circle. Here, the lower-layer trace component not only serves for energy feeding, but also plays a crucial role in defining the geometrical configuration by mechanically interacting with the upper-layer antenna. In particular, the outer regions of the lower-layer feed trace push the antenna upward/outward, such that the resulting 3D configuration more closely resembles a hemispherical shape. Without this feed trace, the 3D structure (Figure 1f, left and right top) deviates evidently from an ideal hemisphere, resulting in inferior antenna performance (e.g., reduced $Q/Q_{\rm lb}$) (Figure S2, Supporting Information).

Electromagnetic simulations and measurements (see the Experimental Section for details) allow quantitative evaluation of the antenna performance. The focus here is on the voltage standing wave ratio (VSWR) characteristics, which determine the impedance-matching with the transmission line.[36] As the magnitude of VSWR approaches 1, the matching approaches an ideal value. The bandwidth (BW) of the antenna can be defined as the frequency range over which the VSWR remains below a specified threshold, and the fractional bandwidth (FBW) is defined as the bandwidth divided by the center frequency. This work uses a VSWR threshold of 5.828, which corresponds to the half-power bandwidth (see the Experimental Section for details).[13] Figure 1g presents the measured and simulated results of VSWR for the device, where good agreements can be observed. In particular, the measured center frequency is 1.08 GHz with a bandwidth of 135 MHz or a fractional bandwidth of 12.5%, consistent with the simulated results (center frequency: 1.085 GHz; bandwidth: 115 MHz; fractional bandwidth: 10.6%). The radiation efficiency is determined as 62% and 64%, according to the measurement and simulation, respectively. The electrical size of this MHESA is $ka = 0.36$, confirming

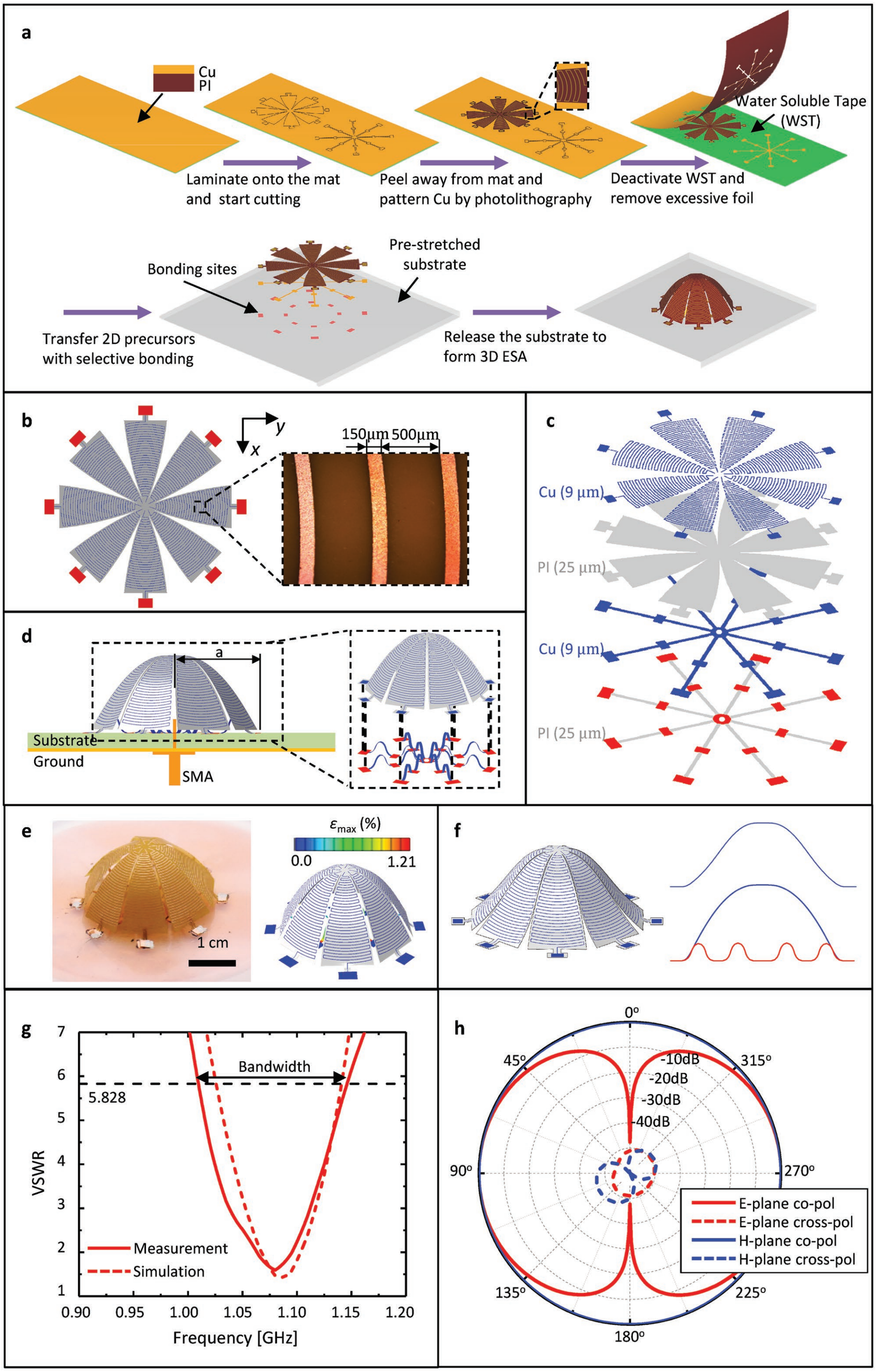

Figure 1. Design, fabrication, experimental measurements, and numerical simulations of meanderline-based hemispherical electrically small antennas (MHESAs). a) Schematic illustration of the fabrication procedures for the MHESA by mechanically guided 3D assembly. b) 2D precursor structure, along with an optical microscopic image of the copper meanderlines. c) Exploded view illustration of the 2D precursor design for the assembly of MHESA, where the red color denotes the bonding sites. d) Schematic illustration of the final 3D configuration of the antenna and the supporting wavy ribbon networks. e) An optical image of the fabricated device and corresponding FEA results with a color scheme that denotes the magnitude of maximum principal strains in the copper layer. f) FEA result of the 3D configuration (left) and a sectional profile (top right) of an antenna without support from the feed trace, along with the profile (bottom right) of its counterpart with the support. g) Measured and simulated voltage standing wave ratio (VSWR) characteristic of the MHESA. h) Simulated radiation patterns (normalized) of the antenna.

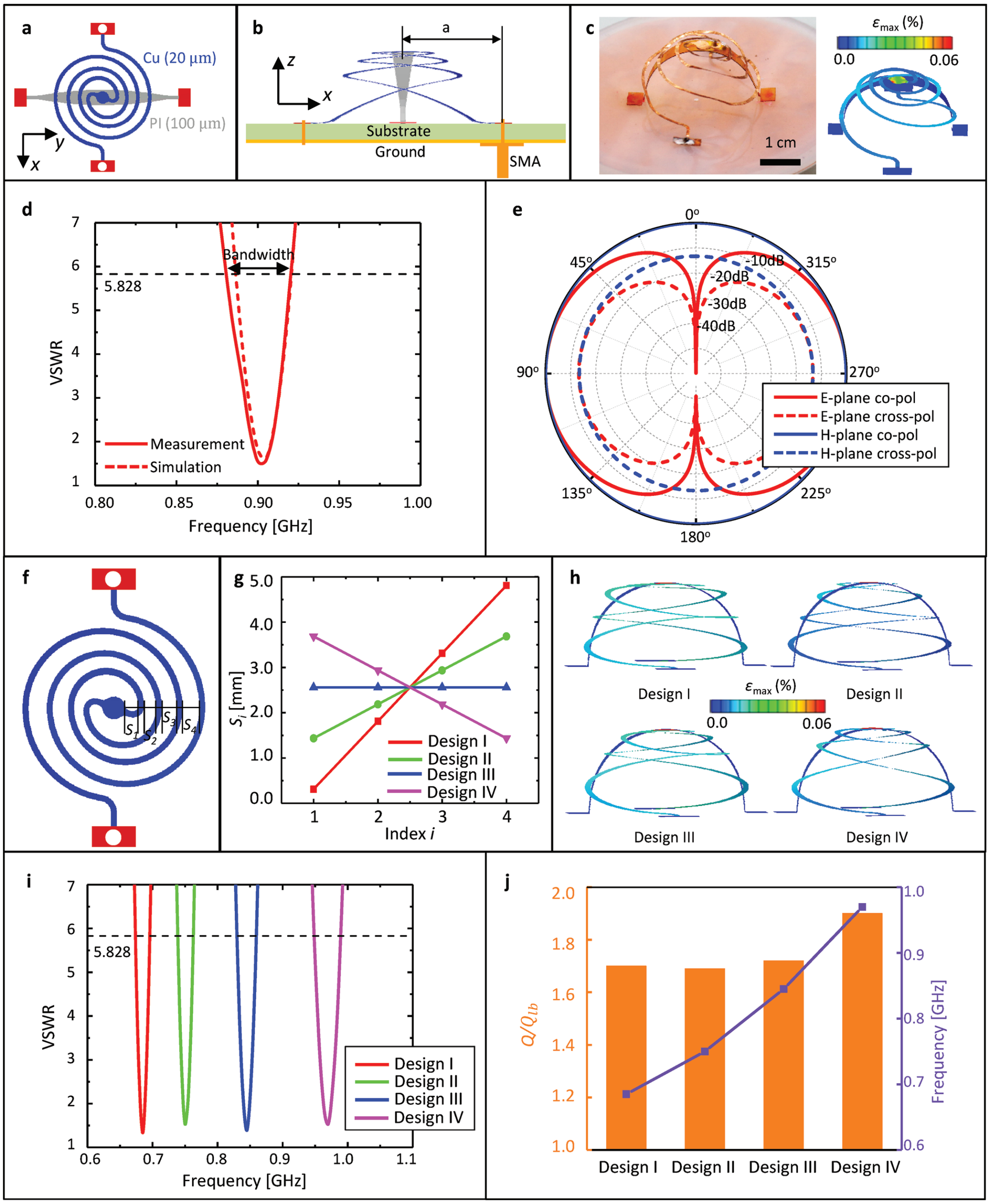

Figure 2. Design, experimental measurements, and numerical simulations of helix-based hemispherical electrically small antennas (HHESAs). a) 2D precursor of the antenna. b) Schematic illustration of the final 3D configuration of the antenna. c) An optical image of the fabricated device and corresponding FEA result. d) Measured and simulated VSWR characteristic of the HHESA. e) Simulated radiation patterns (normalized) of the antenna. f) A representative trace design with illustration of the spacing (S_i). g) Spacing distributions for four trace designs. h) Resulting 3D configurations based on FEA for the four designs. i,j) Simulated Q/Q_{lb} values and VSWR characteristics of the four designs in (h). The bar graph and curve correspond to the left and right vertical axes, respectively. The color of the FEA results in (c) and (h) represents the magnitude of maximum principal strain in the copper layer.

that the antenna is electrically small. According to the equation for Q_{lb} and the relation between Q and FBW, the ratio Q/Q_{lb} is 1.1, which indicates that this MHESA closely approaches the fundamental limit for Q, thereby suggesting nearly optimal performances. For completeness, the normalized radiation patterns obtained by simulation are presented in Figure 1h, and the impedance characteristics based on the measurement and simulation are shown in Figure S3 (Supporting Information).

Figure 2 presents the design concept, experimental measurements, and numerical simulations for another type of hemispherical ESA, i.e., the HHESA, where helical traces form the basis of the structure. The overall fabrication procedure (Figure S4, Supporting Information) is similar to that shown in Figure 1a, although some differences exist, including: 1) the polyimide foil (60 µm in thickness) and copper foil (20 µm in thickness), rather than the bilayered flexible printed circuit board (FPCB), serve as the basis for the 2D precursors; and 2) no photolithography is needed. Figure 2a and Figure S5 (Supporting Information) show the 2D precursor design that consists of two layers—an upper-layer helical trace (copper; 1 mm in width) supported by a lower-layer ribbon (PI) with varying cross-sections and two folding creases at two ends. Euler beam theory allows for accurate selection of the width distribution (see the Experimental Section for details), such that the ribbon forms a nearly perfect arc after compressive buckling.[37] The buckled arc-shaped ribbon can, therefore, serve as a scaffold to be "twined" by the upper-layer helical trace, thereby providing a route to achieve an approximately hemispherical overall shape for the HHESA. Since the HHESA has a helical configuration with two outer ends bonded to the substrate, we connect one end of the HHESA to a SMA terminal for feeding, and electrically short the other end to the metal ground (Figure 2b). The final 3D configuration that results from the use of a uniaxially prestretched elastomer substrate ($\varepsilon_{x-\text{pre}}$ = 0% and $\varepsilon_{y-\text{pre}}$ = 61%; realized by clamping the *x*-directional ends of the substrate to prevent shrinkage induced by the Poission effect) is shown in Figure 2c. The configuration predicted by FEA shows reasonably good agreement with experimental results. Figure 2d summarizes the measured and simulated results of the VSWR characteristics. The measured center frequency is 0.905 GHz, with a half-power bandwidth of 34 MHz or a fractional bandwidth of 3.8%. These values agree well with the simulated results (0.905 GHz, 30 MHz, and 3.3%). Moreover, the measured and simulated radiation efficiencies are 83% and 86%, respectively. Compared with the MHESA (Figure 1), the HHESA has a narrower band, but a higher efficient energy radiation. Although the ratio $Q/Q_{\text{lb}} = 1.6$ of the HHESA is slightly larger than that of the MHESA, the value is still very close to the fundamental limit. The normalized radiation patterns of the HHESA are shown in Figure 2e, and the impedance characteristics based on the measurement and simulation are shown in Figure S6 (Supporting Information).

The geometry of the helical trace is essential in the 2D precursor design of HHESA. Specifically, the helical trace studied here consists of ≈7 semi-circles, with a range of different radii that can be also related to the spacing (S_{i}, as shown in Figure 2f). We consider four representative trace designs (1 mm in width) with different spacing distributions and fixed overall dimensions (L_x and L_y) (see Figure 2g and Figure S7 (Supporting Information) for details). The mechanically assembled 3D configurations are in Figure 2h. The simulated VSWR curves (Figure 2i) suggest a monotonous rightward shift from Designs I to IV. In particular, the center frequency (Figure 2j) can be adjusted in a very wide range (from 0.685 to 0.97 GHz) by tailoring the helical designs. These results follow mainly from a change in the total length of the wire. The ratio Q/Q_{lb} changes only slightly (from 1.69 to 1.90) for the four designs studied herein. This behavior indicates that the detailed 2D helical geometry does not affect the performance significantly, and therefore, the design can be selected simply to achieve the desired center frequency.

It is noteworthy that the designed ESAs can be further miniaturized to meet the requirements of different targeted applications. To demonstrate such capability of device miniaturization, we studied numerically the performance of the antennas (MHESA and HHESA) whose lateral dimensions are scaled down by five times in comparison to those in Figures 1 and 2. The simulated VSWR characteristics of the miniaturized antennas are shown in Figure S8 (Supporting Information). According to these simulations, the radiation efficiency is 60.1% for MHESA and 77.3% for HHESA. The ratio Q/Q_{lb} is then calculated as 1.3 and 1.7 for MHESA and HHESA, respectively. These values of ratio Q/Q_{lb} for the miniaturized antennas are comparable to those of the aforementioned ones and also close to the fundamental limit. These results suggest that the excellent performance of designed ESAs can be maintained at smaller length scales.

The 3D ESAs formed in this manner can be easily reshaped by mechanically deforming the elastomer substrate, thereby providing straightforward means to tune operating frequency. Taking the MHESA as an example, the structure can be transformed reversibly into different 3D configurations, via application of different levels of equal-biaxial tensile strain ($\varepsilon_{\text{appl}}$) to the elastomer substrate. **Figure 3**a (from left to right) shows optical images and FEA predictions of an MHESA under applied tensile strains of 0%, 9%, 18%, and 30%, respectively. The height of the structure decreases with increasing strain, and reduces to 35% of that at the fully assembled state as $\varepsilon_{\text{appl}}$ reaches 30%, indicating that the antenna is sufficiently stretched to demonstrate its tunability. The measured key characteristics (e.g., center frequency, bandwidth, quality factor, radiation efficiency, Q/Q_{lb}, etc.) of the MHESA under different applied strains are summarized in **Table 1**, and the corresponding VSWR curves are shown in Figure 3b. This set of results demonstrates that the best Q/Q_{lb} (Figure 3c) occurs at the fully assembled configuration, where the shape is closest to a hemisphere. The center frequency can be tuned continuously and reversibly in the range of 1.08–0.935 GHz, by applying a tensile strain within 30%. Figure 3d–f and **Table 2** summarize collective results for HHESA, showing mechanical tunability of the 3D configuration and working frequency. Here, a uniaxial tensile strain ($\varepsilon_{y-\text{appl}}$) up to 38% is applied, while fixing $\varepsilon_{x-\text{appl}}$ as 0%. The resulting center frequency shifts from 0.905 to 0.815 GHz. The normalized radiation patterns and impedance characteristics for these two ESAs at different strain states are shown in Figures S9 and S10 (Supporting Information), respectively.

The 3D ESAs formed through the mechanically guided assembly are highly stretchable and compressible, as shown in **Figure 4**. Cyclic mechanical testing (up to 100 cycles) demonstrates their mechanical robustness under two representative loading conditions: stretching the substrate (Figure 4a) and pressing the antennas (Figure 4b). According to experimental measurements of the antennas at their released configurations (i.e., in the load-free condition, without any hands in the proximity of antenna), the variation of the center frequencies is less than 1% for both the MHESA and HHESA experiencing both types of cycling tests. The excellent robustness of the device can be attributed to the low level of maximum principal strains in

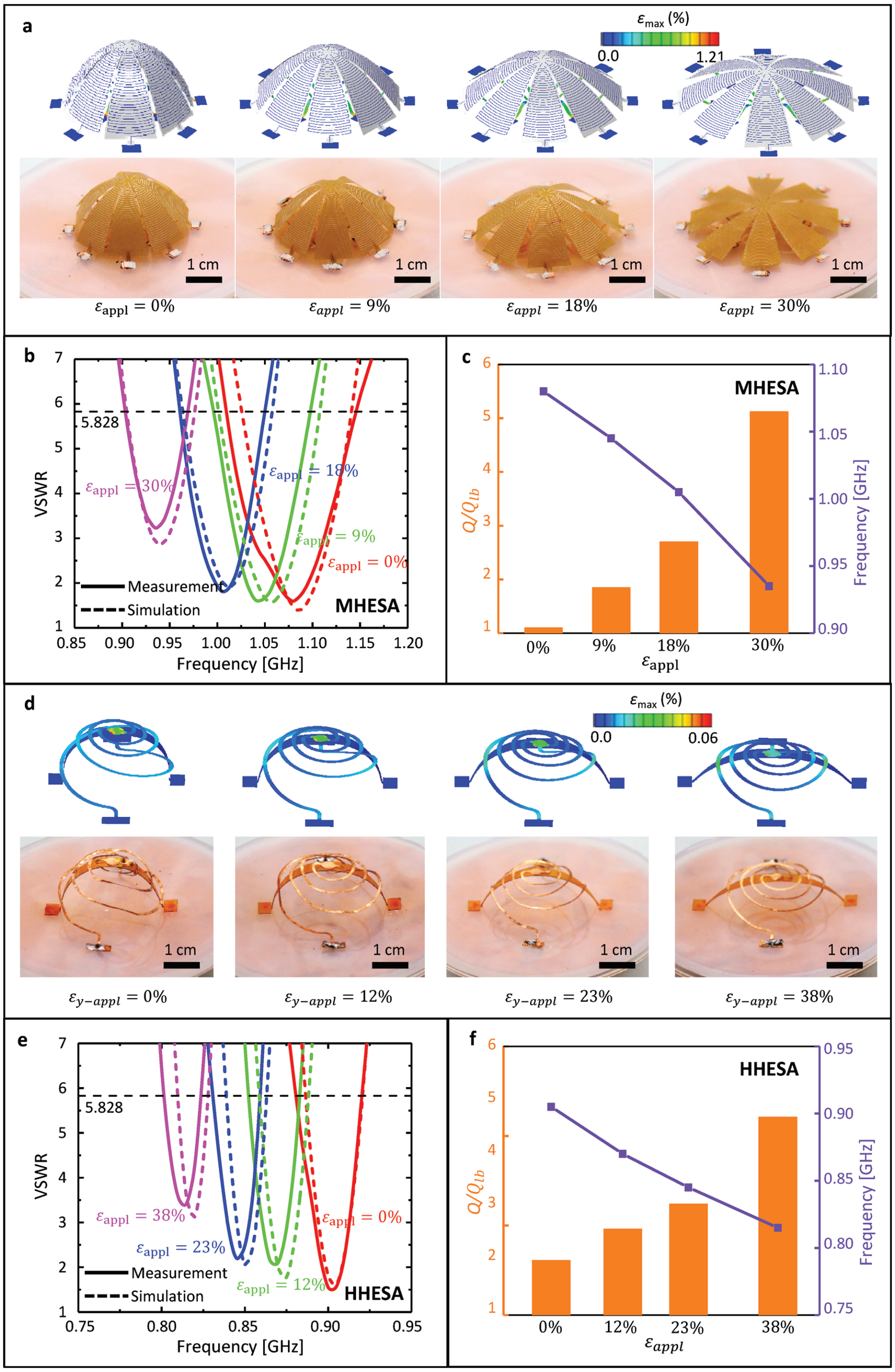

Figure 3. Mechanical tunability of the antennas. a) The MHESA (optical image, bottom; FEA results, top) under equal-biaxial applied tensile strains of 0%, 9%, 18%, and 30%. b) VSWR characteristic of the MHESA under different levels of applied strains. c) Measured Q/Q_{lb} and center frequencies of the MHESA under different levels of applied strains. d) The HHESA (optical image, bottom; FEA results, top) under uniaxial applied tensile strains of 0%, 12%, 23%, and 38%. e) VSWR characteristic of the HHESA under different levels of applied strains. f) Measured Q/Q_{lb} and center frequencies of the HHESA under different levels of applied strains. The color of FEA results in (a) and (d) correspond to the magnitude of maximum principal strain in the copper layer. In (c) and (f), the bar graph and curve correspond to the left and right vertical axes, respectively.

the metal layer, across the range of different mechanical deformations. To further enhance the mechanical robustness for damage prevention, a solid encapsulation might be needed. However, the solid encapsulation typically results in a decreased level of deformability of the 3D devices, due to the mechanical constraints of the surrounding material. To avoid a substantial

Table 1. Radiation characteristics of the MHESA at different strain states.

ε_{appl} [%]	Freq. [GHz]	BW [MHz]	FBW [%]	Q	η_{eff} [%]	ka	Q_{lb}	Q/Q_{lb}
0	1.08	135	12.5	16.0	62	0.36	14.5	1.1
9	1.045	102	9.7	20.5	57	0.39	11.1	1.8
18	1.005	89	8.8	22.5	49	0.41	8.4	2.7
30	0.935	66	7.0	28.5	35	0.42	5.6	5.1

Table 2. Radiation characteristics of the HHESA at different strain states.

ε_{appl} [%]	Freq. [GHz]	BW [MHz]	FBW [%]	Q	η_{eff} [%]	ka	Q_{lb}	Q/Q_{lb}
0	0.905	40	4.4	45.7	83	0.32	28.4	1.6
12	0.87	29	3.4	59.3	79	0.31	30.3	2.0
23	0.845	24	2.8	70.8	76	0.30	31.7	2.2
38	0.815	18	2.2	91.0	61	0.29	28.3	3.2

reduction of the deformability and tunability of the antennas after encapsulation, the utility of an ultrasoft silicone (e.g., Silbione 4717A/B, Bluestar Silicones, France) to serve as the encapsulation material could provide a possible solution.[38] The capability of 3D ESAs to resist joule heating is also experimentally studied for both the MHESA and HHESA, through use of an infrared camera (Flir, T440) to capture the temperature distributions. Here, a fixed power of 1.5 W that highly exceeds the level typically required for wireless communication in daily uses like bluetooth is adopted to feed the antenna.[39] According to the measured results (Figure S11, Supporting Information), the maximum temperature is below 46 °C in the antenna, and

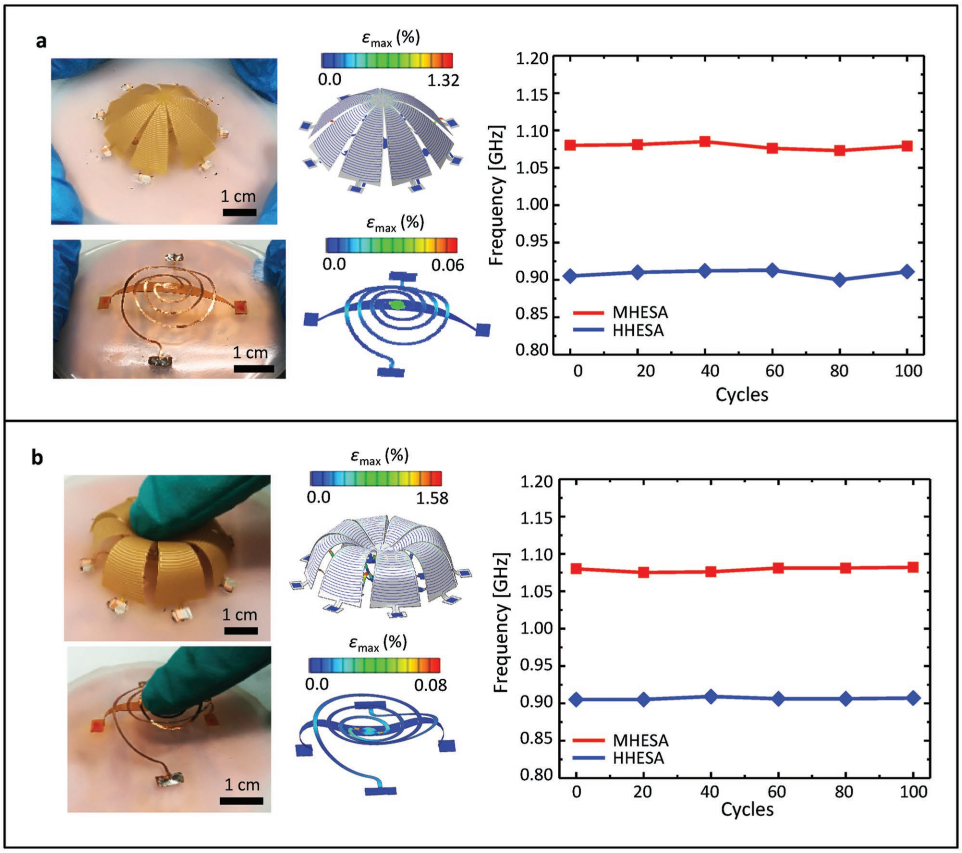

Figure 4. Deformability and mechanical robustness of the fabricated antennas. a) Measured center frequencies of the MHESA/HHESA antennas in their fully assembled configurations during 100 cycles of biaxial/uniaxial tensile strain on the substrates. The images on the left show the deformed configurations of the antennas based on experiments and FEA calculations. b) Measured center frequencies of the antennas in their fully assembled configurations during 100 cycles of pressing and unloading. The images on the left show the deformed configurations of the antennas based on experiments and FEA calculations. The color of the FEA results corresponds to the magnitude of maximum principal strain in the copper layer.

below 40 °C at the substrate surface, for both designs. These results verify the safety and reliability of the antennas in practical applications.

In summary, the results presented here illustrate the utility of mechanically guided 3D assembly in the design and fabrication of two different types of high-quality hemispherical ESAs, i.e., meanderline-based and helix-based hemispherical ESAs. Combined experimental and computational studies highlight the excellent performance characteristics of both systems, as evidenced by their ultralow ratio Q/Q_{lb} (1.1 for MHESA and 1.6 for HHESA). The demonstrated capabilities for tuning the working frequency over a wide range and for sustaining high levels of mechanical deformations suggest promising potential use in many different applications, including those in wireless wearables and biointegrated electronics.[40–47] For such applications related to wearable and biointegrated electronics, the effect of human tissues (e.g., hand, skin) should be considered in the design. For example, the VSWR curve shifts left for both MHESA and HHESA, when putting a human hand over the antenna at a distance of 1 cm (Figure S12, Supporting Information).

Experimental Section

Fabrication Process of MHESA: The fabriation began with a commercial FPCB (a bilayer of PI (25 µm) and copper (Cu, 9 µm), DuPont) laminated on a water soluble tape (WST) with PI facing the WST, adhered to a cutting mat. A programmable cutting machine (Silhouette Cameo) carved the FPCB into desired shapes. Gently peeling the WST/FPCB from the mat and performing photolithographic wet etching further patterned the Cu layer into required geometries. Dipping into water deactivated the WST and allowed separation of the 2D precursor FPCB. The next step involved transferring the precursor onto a prestretched elastomer substrate (Dragon Skin, Smooth-On) and selectively bonding it at predefined locations (bonding sites) with a commercial adhesive (Super Glue, Gorilla Glue Company). Slowly releasing the prestrain completed the assembly of the MHESA.

Measurement of the Antennas: All the antennas were measured with a network analyzer (E5071B, Agilent). The VSWR and center frequency were read directly from this instrument after connecting the antenna to the instrument with a coaxial cable. The radiation efficiency was measured using the Wheeler Cap method.[48,49]

Calculation of Quality Factor (Q): The quality factor (Q) is related to FBW by $Q=(\nu-1)/(\mathrm{FBW}\cdot\sqrt{\nu})$, where ν is the VSWR threshold that defines the BW. The half-power bandwidth for results reported here corresponds to a VSWR threshold of 5.828. Note that the half-power means that 50% of the incident power to the antenna is reflected back to the source. Given the equation above, Q can be determined using the value of FBW.

The Supporting Ribbon in HHESA: Optimized designs with varying width and two folding creases on both ends near the bonding sites ensured that the ribbon formed a nearly perfect arc shape. The folding creases were crafted by carving a nonpenetrating trench with ≈45 µm in depth. And the width w, obtained based on the Euler beam theory, adopted the following distribution

$$w(s)=w_{\max}\frac{\cos\left(\frac{\theta}{2}-\frac{s\theta}{L}\right)-\cos\left(\frac{\theta}{2}\right)}{1-\cos\left(\frac{\theta}{2}\right)},\ \theta=\pi \tag{1}$$

where the s is the natural coordinate, $w_{\max}$ is the specified maximum width of the ribbon, and the θ is the central angle of the arc (here we set θ as 180°, since the semi-circle arc is more appealing to our applications). All these parameters are defined in Figure S5 (Supporting Information).

Mechanics Simulations: FEA exploited the commercial software ABAQUS by using conventional static analysis to simulate the compressive buckling processes. Eight-node 3D solid elements (C3D8R) and four-node shell elements (S4R) were used to model the silicone substrate and 2D precursors, respectively. Convergence of mesh sizes was tested to ensure computational accuracy. The critical buckling strains and corresponding buckling modes determined from linear buckling analyses were implemented as initial imperfections in the postbuckling calculations to obtain the deformed 3D configurations and strain distributions. The elastic modulus (E) and Poisson's ratio (ν) are $E_{\mathrm{substrate}}=166$ kPa and $\nu_{\mathrm{substrate}}=0.49$ for substrate; $E_{\mathrm{Cu}}=119$ GPa and $\nu_{\mathrm{Cu}}=0.34$ for copper; and $E_{\mathrm{PI}}=2.5$ GPa and $\nu_{\mathrm{PI}}=0.34$ for PI.

Electromagnetic Simulations: The finite element method was adopted in electromagnetic simulations to calculate the VSWR, radiation efficiency, and radiation patterns of the antennas. The simulations were conducted using the commercial software ANSYS HFSS, in which tetrahedron elements with adaptive meshing convergence were used. The 3D configurations of the antennas determined by the mechanics simulations were imported to the software ANSYS HFSS. For the sake of efficiency, all the metal layers in the devices, including the antennas themselves and the metal ground plane underneath the substrate, are modeled by layered impedance boundary with prescribed thicknesses; and all the PI layers in the devices were ignored due to their negligible influence on the simulation results. The relative permittivity (ε_{r}), relative permeability (μ_{r}), and conductivity (σ) are $\varepsilon_{\mathrm{r\text{-}Cu}}=1$, $\mu_{\mathrm{r\text{-}Cu}}=0.999991$ and $\sigma_{\mathrm{Cu}}=5.8\times10^{7}$ S m^{-1} for copper; $\varepsilon_{\mathrm{r\_substrate}}=2.55$, $\mu_{\mathrm{r\_substrate}}=1$, and $\sigma_{\mathrm{substrate}}=2.5\times10^{-14}$ S m^{-1} for substrate.

Supporting Information

Supporting Information is available from the Wiley Online Library or from the author.

Acknowledgements

Y.Z. acknowledges the support from the National Natural Science Foundation of China (Grant Nos. 11672152 and 11722217), and the Tsinghua National Laboratory for Information Science and Technology. X.F. acknowledges support from the National Natural Science Foundation of China (Grant No. 11320101001) and the National Basic Research Program of China (Grant No. 2015CB351900). Y.H. acknowledges the support from NSF (Grant Nos. 1400169, 1534120, and 1635443). J.A.R. acknowledges support from the Center for Bio-Integrated Electronics at Northwestern University.

Conflict of Interest

The authors declare no conflict of interest.

Keywords

3D assembly, buckling, electrically small antennas, quality factor, tunability

Received: October 1, 2018
Revised: November 16, 2018

---

[1] C. Yu, Z. Wang, H. Yu, H. Jiang, *Appl. Phys. Lett.* **2009**, *95*, 141912.
[2] D. Son, J. Lee, S. Qiao, R. Ghaffari, J. Kim, J. E. Lee, C. Song, S. J. Kim, D. J. Lee, S. W. Jun, S. Yang, M. Park, J. Shin, K. Do,

M. Lee, K. Kang, C. S. Hwang, N. Lu, T. Hyeon, D.-H. Kim, *Nat. Nanotechnol.* **2014**, *9*, 397.

[3] H.-J. Kim, K. Sim, A. Thukral, C. Yu, *Sci. Adv.* **2017**, *3*, e1701114.

[4] Y. Liu, M. Pharr, G. A. Salvatore, *ACS Nano* **2017**, *11*, 9614.

[5] S. Yao, A. Myers, A. Malhotra, F. Lin, A. Bozkurt, J. F. Muth, Y. Zhu, *Adv. Healthcare Mater.* **2017**, *6*, 1601159.

[6] S. Yao, P. Swetha, Y. Zhu, *Adv. Healthcare Mater.* **2018**, *7*, 1700889.

[7] D. Ye, Y. Ding, Y. Duan, J. Su, Z. Yin, Y. A. Huang, *Small* **2018**, *14*, 1703521.

[8] A. D. Yaghjian, S. R. Best, presented at *IEEE Antenn. Propag. Soc. Internat. Symp.,* Columbus, OH, USA, June **2003**.

[9] L. J. Chu, *J. Appl. Phys.* **1948**, *19*, 1163.

[10] J. S. McLean, *IEEE Trans. Antennas Propag.* **1996**, *44*, 672.

[11] H. L. Thal, *IEEE Trans. Antennas Propag.* **2006**, *54*, 2757.

[12] S. R. Best, *IEEE Trans. Antennas Propag.* **2004**, *52*, 953.

[13] J. J. Adams, E. B. Duoss, T. F. Malkowski, M. J. Motala, B. Y. Ahn, R. G. Nuzzo, J. T. Bernhard, J. A. Lewis, *Adv. Mater.* **2011**, *23*, 1335.

[14] C. Pfeiffer, X. Xu, S. R. Forrest, A. Grbic, *Adv. Mater.* **2012**, *24*, 1166.

[15] M. Jobs, K. Hjort, A. Rydberg, Z. Wu, *Small* **2013**, *9*, 3230.

[16] Z. Wu, M. Jobs, A. Rydberg, K. Hjort, *J. Micromech. Microeng.* **2015**, *25*, 027004.

[17] S. R. Best, D. L. Hanna, *IEEE Antennas Propag. Mag.* **2010**, *52*, 47.

[18] H. A. Wheeler, *Proc. IRE* **1958**, *46*, 1595.

[19] B. Y. Ahn, E. B. Duoss, M. J. Motala, X. Guo, S.-I. Park, Y. Xiong, J. Yoon, R. G. Nuzzo, J. A. Rogers, J. A. Lewis, *Science* **2009**, *323*, 1590.

[20] O. S. Kim, *IEEE Trans. Antennas Propag.* **2014**, *62*, 3839.

[21] Z. Wu, M. Jobs, A. Rydberg, K. Hjort, *J. Micromech. Microeng.* **2015**, *25*, 027004.

[22] M. Kong, G. Shin, S.-H. Lee, I. J. Yoon, *Electron. Lett.* **2016**, *52*, 994.

[23] S. Xu, Z. Yan, K.-I. Jang, W. Huang, H. Fu, J. Kim, Z. Wei, M. Flavin, J. McCracken, R. Wang, A. Badea, Y. Liu, D. Xiao, G. Zhou, J. W. Lee, H. U. Chung, H. Cheng, W. Ren, A. Banks, X. Li, U. Paik, R. G. Nuzzo, Y. Huang, Y. Zhang, J. A. Rogers, *Science* **2015**, *347*, 154.

[24] Y. Zhang, Z. Yan, K. Nan, D. Xiao, Y. Liu, H. Luan, H. Fu, X. Wang, Q. Yang, J. Wang, W. Ren, H. Si, F. Liu, L. Yang, H. Li, J. Wang, X. Guo, H. Luo, L. Wang, Y. Huang, J. A. Rogers, *Proc. Natl. Acad. Sci. USA* **2015**, *112*, 11757.

[25] Z. Yan, F. Zhang, F. Liu, M. Han, D. Ou, Y. Liu, Q. Lin, X. Guo, H. Fu, Z. Xie, M. Guo, Y. Huang, J. Kim, Y. Qiu, K. Nan, J. Kim, P. Gutruf, H. Luo, A. Zhao, K.-C. Hwang, Y. Huang, Y. Zhang, J. A. Rogers, *Sci. Adv.* **2016**, *2*, e1601014.

[26] Z. Yan, F. Zhang, J. Wang, F. Liu, X. Guo, K. Nan, Q. Lin, M. Gao, D. Xiao, Y. Shi, Y. Qiu, H. Luan, J. Kim, Y. Wang, H. Luo, M. Han, Y. Huang, Y. Zhang, J. A. Rogers, *Adv. Funct. Mater.* **2016**, *26*, 2629.

[27] H. Fu, K. Nan, W. Bai, W. Huang, K. Bai, L. Lu, C. Zhou, Y. Liu, F. Liu, J. Wang, M. Han, Z. Yan, H. Luan, Y. Zhang, Y. Zhang, J. Zhao, X. Cheng, M. Li, J. W. Lee, Y. Liu, D. Fang, X. Li, Y. Huang, Y. Zhang, J. A. Rogers, *Nat. Mater.* **2018**, *17*, 268.

[28] O. G. Schmidt, K. Eberl, *Nature* **2001**, *410*, 168.

[29] Y. Mei, G. Huang, A. A. Solovev, E. B. Ureña, I. Mönch, F. Ding, T. Reindl, R. K. Fu, P. K. Chu, O. G. Schmidt, *Adv. Mater.* **2008**, *20*, 4085.

[30] X. Guo, H. Li, B. Y. Ahn, E. B. Duoss, K. J. Hsia, J. A. Lewis, R. G. Nuzzo, *Proc. Natl. Acad. Sci. USA* **2009**, *106*, 20149.

[31] J. S. Randhawa, M. D. Keung, P. Tyagi, D. H. Gracias, *Adv. Mater.* **2010**, *22*, 407.

[32] L. R. Meza, S. Das, J. R. Greer, *Science* **2014**, *345*, 1322.

[33] X. Yu, W. Huang, M. Li, T. M. Comberiate, S. Gong, J. E. Schutt-Aine, X. Li, *Sci. Rep.* **2015**, *5*, 9661.

[34] Q. Guo, Z. Di, M. G. Lagally, Y. Mei, *Mater. Sci. Eng., R* **2018**, *128*, 1.

[35] Y. Zhang, F. Zhang, Z. Yan, Q. Ma, X. Li, Y. Huang, J. A. Rogers, *Nat. Rev. Mater.* **2017**, *2*, 17019.

[36] K. B. Schaub, J. Kelly, *Production Testing of RF and System-on-a-chip Devices for Wireless Communications*, Artech House, Norwood, MA, USA **2004**.

[37] J. Gere, S. Timoshenko, *Mechanics of Materials*, Pws Pub. Co. Boston, MA, USA **1997**.

[38] K. I. Jang, K. Li, H. U. Chung, S. Xu, H. N. Jung, Y. Yang, J. W. Kwak, H. H. Jung, J. Song, C. Yang, A. Wang, Z. Liu, J. Y. Lee, B. H. Kim, J.-H. Kim, J. Lee, Y. Yu, B. J. Kim, H. Jang, K. J. Yu, J. Kim, J. W. Lee, J.-W. Jeong, Y. M. Song, Y. Huang, Y. Zhang, J. A. Rogers, *Nat. Commun.* **2017**, *8*, 15894.

[39] G. P. Perrucci, H. F. Fitzek, J. Widmer presented at *IEEE Veh. Technol. Conf.*, Yokohama, Japan, May **2011**.

[40] D. H. Kim, J. Viventi, J. J. Amsden, J. Xiao, L. Vigeland, Y. S. Kim, J. A. Blanco, B. Panilaitis, E. S. Frechette, D. Contreras, D. L. Kaplan, F. G. Omenetto, Y. Huang, K.-C. Hwang, M. R. Zakin, B. Litt, J. A. Rogers, *Nat. Mater.* **2010**, *9*, 511.

[41] D. J. Lipomi, M. Vosgueritchian, B. C. Tee, S. L. Hellstrom, J. A. Lee, C. H. Fox, Z. Bao, *Nat. Nanotechnol.* **2011**, *6*, 788.

[42] S. Xu, Y. Zhang, L. Jia, K. E. Mathewson, K. I. Jang, J. Kim, H. Fu, X. Huang, P. Chava, R. Wang, S. Bhole, L. Wang, Y. J. Na, G. Yue, M. Flavin, Z. Han, Y. Huang, J. A. Rogers, *Science* **2014**, *344*, 70.

[43] Y. Chen, B. Lu, Y. Chen, X. Feng, *Sci. Rep.* **2015**, *5*, 11505.

[44] B. Lu, Y. Chen, D. Ou, H. Chen, L. Diao, W. Zhang, J. Zheng, W. Ma, L. Sun, X. Feng, *Sci. Rep.* **2015**, *5*, 16065.

[45] S. I. Park, D. S. Brenner, G. Shin, C. D. Morgan, B. A. Copits, H. U. Chung, M. Y. Pullen, K. N. Noh, S. Davidson, S. J. Oh, J. Yoon, K. I. Jang, V. K. Samineni, M. Norman, J. G. Grajales-Reyes, V. S. K. , S. S. Sundaram, K. M. Wilson, J. S. Ha, R. Xu, T. Pan, T. I. Kim, Y. Huang, M. Montana, J. P. Golden, M. R. Bruchas, R. W. Gereau IV, J. A. Rogers, *Nat. Biotechnol.* **2015**, *33*, 1280.

[46] S. Yang, Y. C. Chen, L. Nicolini, P. Pasupathy, J. Sacks, B. Su, R. Yang, D. Sanchez, Y. F. Chang, P. Wang, D. Schnyer, D. Neikirk, N. Lu, *Adv. Mater.* **2015**, *27*, 6423.

[47] L. Cai, A. Y. Song, P. Wu, P.-C. Hsu, Y. Peng, J. Chen, C. Liu, P. B. Catrysse, Y. Liu, A. Yang, *Nat. Commun.* **2017**, *8*, 496.

[48] H. A. Wheeler, *Proc. IRE* **1959**, *47*, 1325.

[49] M. Geissler, O. Litschke, D. Heberling, P. Waldow presented at *IEEE Antenn. Propag. Soc. Internat. Symp.*, Columbus, OH, USA, June **2003**.